

# Shadows, Quasinormal Modes, and Optical Appearances of Black Holes in Horndeski Theory

Zhi Luo <sup>a</sup>, Ke-Jian He <sup>a</sup>, Hao Yu <sup>a,b</sup>, Jin Li <sup>a,b<sup>1</sup></sup>

<sup>a</sup> Department of Physics, Chongqing University, Chongqing 401331, China

<sup>b</sup> Department of Physics and Chongqing Key Laboratory for Strongly Coupled Physics, Chongqing University, Chongqing 401331, China

## Abstract

In this study, we investigate the dynamics of photons in black hole (BH) spacetimes within the framework of Horndeski theory, focusing on quasinormal modes (QNMs) and the optical appearances of BHs surrounded by thin accretion disks. We analyze photon motion, derive the effective potential and photon sphere radius, and calculate QNMs using the WKB method and the eikonal limit. Using Event Horizon Telescope (EHT) observations of M87\* and SgrA\*, we constrain the parameter  $-0.46 \lesssim \gamma \lesssim 0.31$  within a  $1\sigma$  confidence interval, providing limits on Horndeski gravity. Additionally, we establish the frequency ranges of the fundamental mode for M87\* and SgrA\* as  $2.4 \times 10^{-6}\text{Hz} \lesssim f \lesssim 2.7 \times 10^{-6}\text{Hz}$  and  $3.6 \times 10^{-3}\text{Hz} \lesssim f \lesssim 4.1 \times 10^{-3}\text{Hz}$ , respectively. We further explore the optical appearances of these BHs, highlighting the dependence on emission characteristics and demonstrating that the current EHT resolution primarily captures direct emission. This work advances our understanding of BH shadows and constrains Horndeski gravity.

---

<sup>1</sup>cqstarv@hotmail.com, the corresponding author

# 1 Introduction

In September 2015, the Laser Interferometer Gravitational-Wave Observatory (LIGO) detectors made their first observation of a gravitational wave (GW) signal, attributed to the merger of two stellar-mass black holes (BHs) [1, 2]. This GW event provided evidence supporting the existence of BHs. Subsequent detections have included GW signals from various events [3–7]. For example, in August 2017, the Advanced LIGO and Advanced Virgo detectors identified the inspiral of a binary neutron star system, GW170817 [7], with a high signal-to-noise ratio of 32.4 and a very low false-alarm rate. This detection, along with others [3–7], has significantly broadened the scope of observational astronomy by offering crucial insights into astrophysics. In addition, in 2019, the Event Horizon Telescope (EHT) collaboration released the first image of the supermassive BH at the center of the M87\* galaxy [8–13]. This marked the first time in history that humanity has directly "observed" a BH. Subsequently, the EHT collaboration also published the image of the supermassive BH at the center of our Milky Way galaxy, SgrA\* [14–19]. The images depict a dark region surrounded by a bright ring, which represents the BH shadow formed by the critical curve [20, 21]. As photons from distant sources pass near the BH, their paths bend due to the strong gravitational field near the BH. Photons with smaller impact parameters fall into the BH, while those with larger impact parameters escape. Studies of BH shadows reveal that non-rotating BHs produce circular shadows [22, 23], while rotating BHs exhibit distorted shadows due to dragging effect effects caused by their spin [24–26]. In recent years, the BH shadow within modified gravity theories has garnered widespread attention and extensive research [27–56].

We can study the final stage of GW signals, the ringdown phase, using BH perturbation theory, which is described by quasinormal modes (QNMs). There are two approaches to investigate perturbations within BH spacetimes: one focuses on fields within the BH spacetime, such as a massless scalar field in the BH background, and the other considers perturbations of the BH's own spacetime structure. Research has shown that QNMs are related to BH shadows [57–64]. In the eikonal limit, the real part of the QNMs is proportional to the angular velocity of the unstable circular null geodesics, while the imaginary part is related to the Lyapunov exponent of the unstable circular null geodesics. Given that the optical appearance of BHs is closely related to the unstable circular null geodesics, it can be inferred that the real part of the QNMs is connected to the size of the BH shadow, a relationship that has been studied in Refs. [65–80]. Furthermore, because astrophysical BHs are typically surrounded by significant amounts of accreting material, various accretion disk models have been proposed to study the optical appearance of BHs [20, 23, 81–88]. Inspired by these works, we study the shadow of BHs in Horndeski theory, their QNMs, and their optical appearances when surrounded by thin accretion disks. Additionally, we use observational data from the EHT to constrain Horndeski gravity and provide the frequency ranges of the fundamental mode for M87\* and SgrA\*.

A most general scalar-tensor theory characterized by second-order derivative field equations was constructed by Horndeski [89]. Horndeski theory is a significant scalar-tensor framework that integrates various gravity theories such as General Relativity, quintessence,  $k$ -essence, and others [90–92]. Moreover, Gleyzes *et al.* proposed an extension to this framework, known as "beyond Horndeski theory," designed to mitigate Ostrogradski instabilities [93, 94]. Subsequently, Babichev *et al.* discovered spherical, symmetric, and static BH solution within both shift-symmetric Horndeski and beyond Horndeski theories [95]. Recently, the studies of BHs within these Horndeski and beyond Horndeski theories have seen substantial scholarly interest [95–104]. In this paper, we study the shadow of BHs in Horndeski theory, their QNMs, and their optical appearances.

This paper is organized as follows. In Sec. 2, we analyze the motion of photons in the BH spacetime background, deriving the effective potential, critical impact parameter, and photon sphere

radius. We explore how the parameter  $\gamma$  influences these properties and use EHT observational data for M87\* and SgrA\* to constrain the parameter  $\gamma$ . In Sec. 4, we study the perturbations of a scalar field in the BH background, calculating the QNMs using the WKB method and eikonal limit. We examine the impact of  $\gamma$  on the QNMs and their relation to the shadow radius. In Sec. 3, we examine the optical appearances of the BH surrounded by a thin accretion disk and compare these theoretical models with images obtained from the EHT. In Sec. 5, we provide our conclusions. Throughout this paper, we adopt natural units where  $G = 1 = c$ .

## 2 Shadow of the BH in Horndeski theory

The action within Horndeski theory is given by [95]

$$S = \int d^4x \sqrt{-g} (\mathcal{L}_2 + \mathcal{L}_3 + \mathcal{L}_4 + \mathcal{L}_5), \quad (1)$$

where  $\mathcal{L}_i$  represent the Lagrangian densities. For the spherically symmetric metric of the BH solution in Horndeski theory, the corresponding line element takes the form [95]

$$ds^2 = -f(r)dt^2 + \frac{1}{f(r)}dr^2 + r^2(d\theta^2 + \sin^2\theta d\phi^2), \quad (2)$$

where

$$f(r) = 1 - \frac{2M}{r} - \frac{\beta^2}{2\zeta\eta r^2}. \quad (3)$$

Here,  $M$  is an integration constant that represents the BH mass. The parameters  $\eta$  and  $\beta$  are dimensionless and share the same sign, while  $\zeta$  is given by  $M_{\text{Pl}}^2/(16\pi)$ . Note that  $\beta^2/(2\zeta\eta)$  can be regarded as a whole, one can introduce a new parameter  $\gamma = \beta^2/(2\zeta\eta)$  for the sake of simplicity. Thus, we can reformulate Eq. (3) as

$$f(r) = 1 - \frac{2M}{r} - \frac{\gamma}{r^2}. \quad (4)$$

When the parameter  $\gamma$  takes on the negative value,  $\sqrt{-\gamma}$  behaves similarly to an electric charge of the Reissner-Nordström BH. Furthermore, the radius of the outer event horizon can be determined by solving the equation  $f(r_h) = 0$ , yielding  $r_h = M + \sqrt{M^2 + \gamma}$ . To avoid the formation of a naked singularity, it is essential to ensure that  $\gamma \geq -M^2$ . In the case of  $\gamma = -M^2$ , the solution (2) represents an extremal BH. The metric function (4) is illustrated in Fig. 1. It is evident that for  $\gamma > 0$  and in the Schwarzschild case, only a single horizon is formed. In contrast, for  $-M^2 < \gamma < 0$ , both inner and outer horizons are present. This plot clearly illustrates the influence of the parameter  $\gamma$  on the black hole solution.

To study the black hole shadow within the framework of Horndeski theory, we utilize the Lagrangian to derive the equation of motion for the photon, which is given by:

$$\mathcal{L} = \frac{1}{2}g_{\mu\nu}\dot{x}^\mu\dot{x}^\nu = \frac{1}{2}\left(-f(r)\dot{t}^2 + \frac{\dot{r}^2}{f(r)} + r^2(\dot{\theta}^2 + \sin^2\theta\dot{\phi}^2)\right). \quad (5)$$

Here,  $\dot{x} \equiv dx/d\lambda$  and  $\lambda$  is the affine parameter. Considering only the photon moving on the equatorial plane (i.e.  $\theta = \pi/2$  and  $\dot{\theta} = 0$ ), and given that the Lagrangian (5) does not depend on the time coordinate  $t$  or the azimuthal angle  $\phi$ , we can derive two conserved quantities:

$$p_t = \frac{\partial \mathcal{L}}{\partial \dot{t}} = f(r)\dot{t} = E, \quad p_\phi = -\frac{\partial \mathcal{L}}{\partial \dot{\phi}} = r^2\dot{\phi} = L. \quad (6)$$

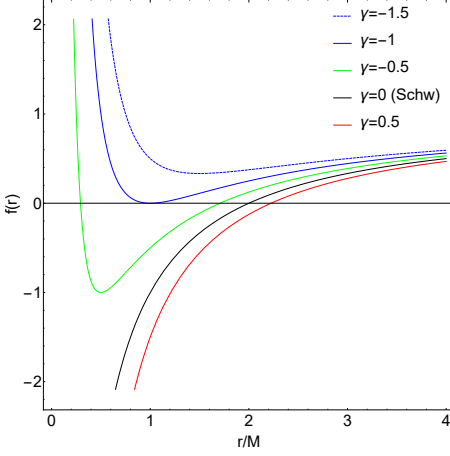


Figure 1: The metric functions  $f(r)$  of BHs in Horndeski theory for various values of the parameter  $\gamma$ . We set  $M = 1$ .

In addition, we can obtain the four-velocity of the time, radial, and azimuthal components as follows:

$$\dot{t} = \frac{1}{b} f(r)^{-1}, \quad \dot{r} = \sqrt{\frac{1}{b^2} - \frac{1}{r^2} f(r)}, \quad \dot{\phi} = \pm \frac{1}{r^2}, \quad (7)$$

in which  $\pm$  indicates the direction of photon motion, with  $+$  representing clockwise and  $-$  indicating counterclockwise. The parameter  $b$  represents the impact parameter, defined as  $b = |L|/E$ . Using Eq. 7, we can obtain

$$\dot{r}^2 + V_{\text{eff}} = \frac{1}{b^2} \quad (8)$$

with

$$V_{\text{eff}} = \frac{1}{r^2} f(r). \quad (9)$$

Here,  $V_{\text{eff}}$  denotes the effective potential, which meets the condition for the photon's unstable circular orbit as follows:

$$V_{\text{eff}}(r_{\text{ph}}) = \frac{1}{b_c^2}, \quad V'_{\text{eff}}(r_{\text{ph}}) = 0, \quad (10)$$

in which  $r_{\text{ph}}$  denotes the radius of the photon sphere,  $b_c$  is the critical impact parameter. In the context of spacetime (2), we can obtain the analytical expressions of  $r_{\text{ph}}$  and  $b_c$ ,

$$r_{\text{ph}} = \frac{1}{2} \left( 3M + \sqrt{9M^2 + 8\gamma} \right), \quad (11)$$

$$b_c = \frac{\sqrt{27M^4 + 36M^2\gamma + 8\gamma^2 + 9M^3\sqrt{9M^2 + 8\gamma} + 8M\gamma\sqrt{9M^2 + 8\gamma}}}{\sqrt{2}\sqrt{M^2 + \gamma}}. \quad (12)$$

It shows that the photon sphere radius and critical impact parameter depend on the BH mass and the parameter  $\gamma$ , as illustrated in Fig. 2. With a constant BH mass, an increase in the parameter  $\gamma$  results in an increase in the event horizon radius, photon sphere radius, and critical impact parameter. This indicates that  $r_h$ ,  $r_{\text{ph}}$ , and  $b_c$  are positively correlated with  $\gamma$ .

Fig. 3 illustrates the effective potential of the BH for different values of the parameter  $\gamma$ . Considering  $\gamma = -0.2$  as an example, we observe that the effective potential rises from the event horizon,

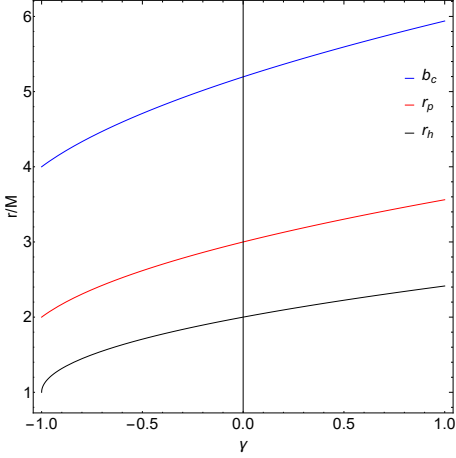


Figure 2: The event horizon radius, photon sphere radius, and critical impact parameter vary with different values of the parameter  $\gamma$ . We set  $M = 1$ .

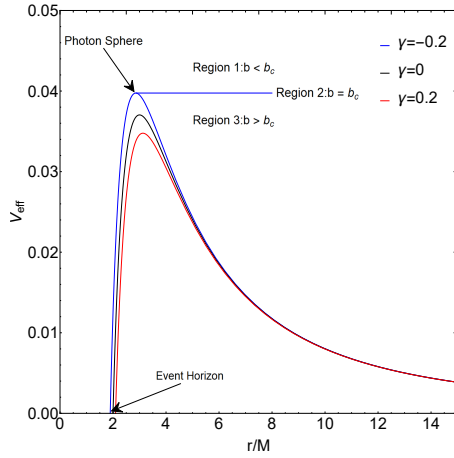


Figure 3: Effective potentials of the BH with parameters  $\gamma = -0.2, 0, 0.2$ . We set  $M = 1$ .

reaches a peak at the photon sphere radius, and then declines. Additionally, Fig. 3 demonstrates that as the parameter  $\gamma$  increases, the peak value of the effective potential decreases.

To thoroughly study the trajectory of the photon, we rewrite the photon's equation of motion using Eq. (7), which is as follows:

$$\frac{dr}{d\phi} = \pm r^2 \sqrt{\frac{1}{b^2} - \frac{1}{r^2} \left(1 - \frac{2M}{r} - \frac{\gamma}{r^2}\right)} \quad (13)$$

With a coordinate transformation  $x \equiv 1/r$ , Eq. (13) can be expressed as

$$\mathcal{G}(x, b) \equiv \frac{dx}{d\phi} = \sqrt{\frac{1}{b^2} - x^2 (1 - 2Mx - \gamma x^2)}. \quad (14)$$

Eq. 14 can be utilized to determine the trajectory of photons on the equatorial plane. When a photon with an impact parameter  $b$  approaches the BH from infinity, one of three scenarios will occur [20]:

- $b < b_c$  Photons heading directly towards the center of the BH will follow a straight trajectory and fall into the BH, while other photons will follow curved trajectories and also be captured by the BH. For the event horizon of  $r_0 = 1/x_0$ , the total deflection angle for photons is given by

$$\phi = \int_0^{x_0} \frac{dx}{\sqrt{\mathcal{G}(x, b)}}. \quad (15)$$

- $b = b_c$  Photons moving toward the BH reach the critical point  $u_c$  and then orbit the BH along a circular path with a radius  $r_{ph}$ . In this scenario, the motion of the photons is in a critical state, and these photons delineate the boundary of the BH shadow.
- $b > b_c$  Photons approach the BH along curved trajectories, reaching the nearest point  $x_{min}$  (the smallest positive real root of  $\mathcal{G}(x, b) = 0$ ), and then escape to infinity. The corresponding total deflection angle is given by

$$\phi = 2 \int_0^{x_{min}} \frac{dx}{\sqrt{\mathcal{G}(x, b)}}. \quad (16)$$

In Fig. 4, we plot the trajectories of photons in polar coordinates for different values of the parameter  $\gamma = -0.3, 0, 0.3$ . Here, the impact parameter  $b$  can be considered as the vertical distance between the photon's geodesic and the parallel line that intersect the origin. When the impact parameter  $b < b_c$  (Region 1 in Fig. 3), the photons will be captured by the BH, and these trajectories correspond to the black lines shown in Fig. 4. When  $b = b_c$  (Region 2 in Fig. 3), the photons will orbit the BH an infinite number of times, and their trajectories are represented by the red ring in Fig. 3. When  $b > b_c$  (Region 3 in Fig. 3), the photons will be reflected back and move to infinity, following the paths that corresponds to the blue lines in Fig. 3. According to Eq. (12), the critical impact parameter  $b_c$  depends only on the parameter  $\gamma$  and the mass  $M$  of the BH. This indicates that for a fixed mass, the size of the BH shadow is solely determined by the parameter  $\gamma$ .

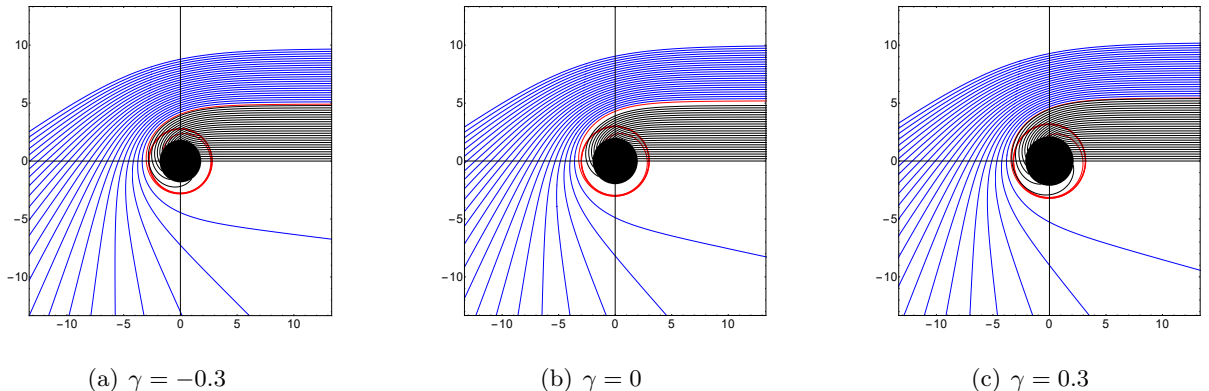


Figure 4: Trajectories of photons for different parameters  $\gamma = -0.3, 0, 0.3$  in polar coordinates  $(r, \phi)$ . The red ring represents to the critical curve, the black hole is depicted as a black disk, with black curves and blue curves representing the cases where  $b < b_c$  and  $b > b_c$ , respectively. We set  $M = 1$  and select the spacing of the impact parameter  $b$  to be  $1/5$ .

Furthermore, by comparing the BH shadow in Horndeski theory with the observed shadows of the supermassive BH M87\* and SgrA\* captured by the EHT collaboration [8–19], we can constrain

the value of the parameter  $\gamma$ . For a static observer located at position  $r_0$ , the shadow radius of the black hole can be expressed by [19, 113, 114]

$$\mathcal{R}_{\text{sh}} = r_{\text{ph}} \sqrt{\frac{f(r_0)}{f(r_{\text{ph}})}}, \quad (17)$$

in which  $f(r_0) = 1$  for a large distant observer. Then we can obtain the shadow diameter  $d_{\text{sh}}^{\text{Horndeski}} = 2\mathcal{R}_{\text{sh}}$  for the BH in Horndeski theory. Meanwhile, when expressed in units of the BH mass, the diameter of the BH shadow is

$$d_{\text{sh}} = \frac{D\theta}{M}. \quad (18)$$

Based on the papers from the EHT [8, 16], the angular diameter of the shadow for M87\* is  $\theta_{\text{M87}^*} = (42 \pm 3) \mu\text{as}$ , its distance from the Earth is  $D_{\text{M87}^*} = 16.8^{+0.8}_{-0.7} \text{Mpc}$ , and its mass is  $M_{\text{M87}^*} = (6.5 \pm 0.9) \times 10^9 M_\odot$ . For the SgrA\*, the shadow angular diameter is  $\theta_{\text{Sgr.A}^*} = (48.7 \pm 7) \mu\text{as}$ , its distance is  $D_{\text{Sgr.A}^*} = 8277 \pm 33 \text{pc}$ , and its mass is  $M_{\text{Sgr.A}^*} = (4.3 \pm 0.013) \times 10^6 M_\odot$ . Hence, the diameters of the shadow images of M87\* and Sgr.A\* are  $d_{\text{sh}}^{\text{M87}^*} = (11 \pm 1.5)$  and  $d_{\text{sh}}^{\text{Sgr.A}^*} = (9.5 \pm 1.4)$ , respectively. In Fig. 5, we present the constraints on the parameter  $\gamma$  derived from the EHT observations of M87\* and SgrA\*. Based on the  $1\sigma$  and  $2\sigma$  confidence intervals for  $d_{\text{sh}}^{\text{M87}^*}$ , the parameter  $\gamma$  is constrained to  $-0.46 \lesssim \gamma \lesssim 1.50$  at  $1\sigma$  and  $-1.00 \lesssim \gamma \lesssim 2.92$  at  $2\sigma$ . For  $d_{\text{sh}}^{\text{Sgr.A}^*}$ , the parameter  $\gamma$  is constrained to  $-0.97 \lesssim \gamma \lesssim 0.31$  at  $1\sigma$  and  $-1.12 \lesssim \gamma \lesssim 1.34$  at  $2\sigma$ . The constraints on the parameter  $\gamma$  from SgrA\* are more stringent compared to those obtained from M87\*. The constraint on the upper limit of the parameter  $\gamma$  obtained from SgrA\* is stricter than that derived from M87\*. Conversely, the constraint on the lower limit of the parameter  $\gamma$  from M87\* is stringent than that from SgrA\*.

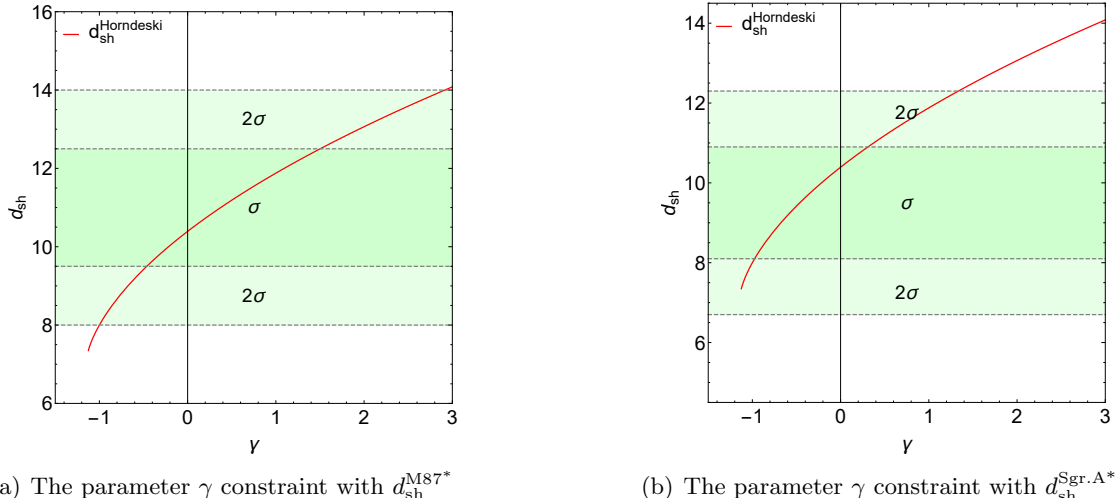


Figure 5: Shadow diameter  $d_{\text{sh}}^{\text{Horndeski}}$  (red lines) of the BH in Horndeski theory as a function of the parameter  $\gamma$ . The shaded areas represent the value of  $d_{\text{sh}}^{\text{Horndeski}}$  that consists with the shadow diameters of the M87\* and SgrA\* as observed by the EHT. The green shaded region indicates the  $1\sigma$  confidence interval for  $d_{\text{sh}}^{\text{Horndeski}}$ , while the light green shaded areas denotes the  $2\sigma$  confidence interval. We set  $M = 1$ .

### 3 QNMs and the eikonal limit for the BH in Horndeski theory.

In this section, we examine the QNMs of the massless scalar field perturbation for the BH in Horndeski theory, comparing these results with the QNMs in the eikonal limit. Additionally, we utilize the EHT data presented in Sec. 2 to determine the oscillation frequencies for M87\* and SgrA\*.

#### 3.1 QNMs of the massless scalar field perturbation

Within the spacetime described by Eq. (2), we utilize the Klein-Gordon equation to analyze a massless scalar field  $\Phi$ , which is given by

$$\frac{1}{\sqrt{-g}} \partial_\mu (\sqrt{-g} g^{\mu\nu} \partial_\nu \Phi) = 0 \quad (19)$$

with

$$\Phi = e^{-i\omega t} Y_{lm}(\theta, \varphi) \frac{\Psi(r)}{r}, \quad (20)$$

in which  $g_{\mu\nu}$  denotes the metric tensor, and  $g$  is its determinant. With a coordinate transformation  $dr_* \equiv dr/f(r)$ , we can get

$$\frac{d^2\Psi(r_*)}{dr_*^2} + [\omega^2 - V_S(r)] \Psi(r_*) = 0, \quad (21)$$

where

$$V_S(r) = f(r) \left( \frac{\ell(\ell+1)}{r^2} + \frac{f'(r)}{r} \right). \quad (22)$$

Here,  $V_S(r)$  denotes the effective potential for the massless scalar field perturbation,  $\ell$  is the multipole number, and  $\omega$  is the complex quasinormal mode (QNM) frequency. We use the 6th-order WKB method to calculate the QNM frequencies of the massless scalar field perturbation, which is as follows [115–117]:

$$\frac{i(\omega^2 - V_{max})}{\sqrt{-2V''_{max}}} - \sum_{i=2}^6 \Lambda_i = n + \frac{1}{2}, \quad (23)$$

where  $n$  represents the overtone number,  $V_{max}$  and  $V''_{max}$  are the values of the potential and its 2nd derivative with respect to  $r_*$  in the maximum, respectively.  $\Lambda_i$  is the  $i$ th-order correction term, which is given in [115–117]. In the following study, we will concentrate on the fundamental QNMs with the overtone number  $n = 0$  and multipole number  $\ell = 2$ .

Based on the EHT data for the M87\* and SgrA\*, the QNM frequencies with for different values of the parameter  $\gamma$  at  $1\sigma$  confidence interval are calculated. In addition, The real and negative imaginary parts of the QNM frequencies are shown in Fig. 6. As the parameter  $\gamma$  increases, both the real part and the negative imaginary part decrease monotonically. This implies that for the smaller parameter  $\gamma$ , the scalar wave oscillates more frequently.

#### 3.2 QNMs in the eikonal limit

In the eikonal limit  $\ell \gg 1$ , Cardoso et al. [58] suggest an unstable circular null geodesic method to calculate the QNMs of a BH, which is given by [58, 118, 119]

$$\omega = \Omega_c \ell - i(n + 1/2) |\lambda_L|, \quad (24)$$

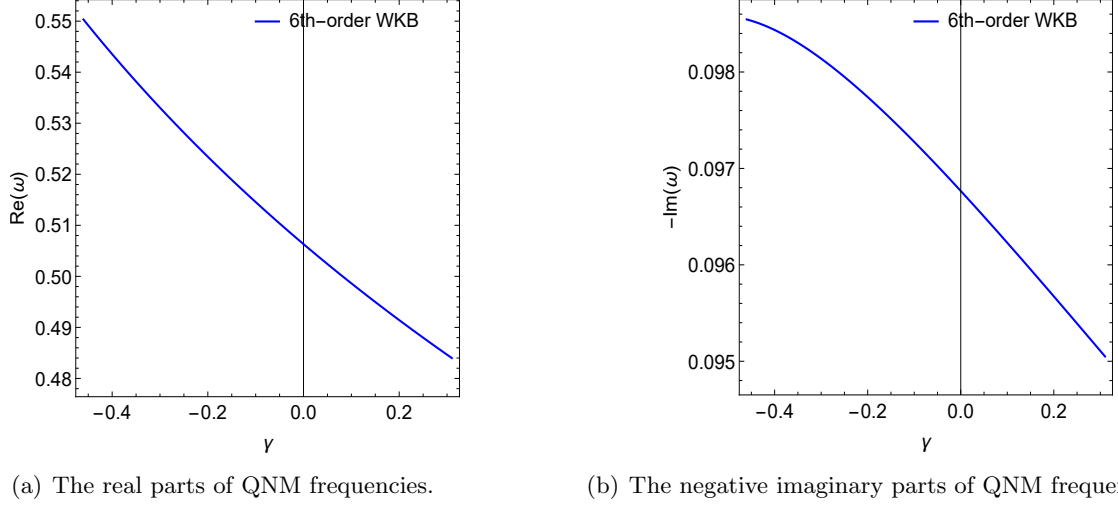


Figure 6: The real and negative imaginary parts of the QNM frequencies calculated via the 6th-order WKB method. The parameter  $-0.46 \lesssim \gamma \lesssim 0.31$  at  $1\sigma$  confidence interval based on the EHT data. We set the overtone number  $n = 0$ , the multipole number  $\ell = 2$ , and  $M = 1$ .

where

$$\Omega_c = \frac{\sqrt{f(r_c)}}{r_c}, \quad \lambda_L = \sqrt{\frac{f(r_c)[2f(r_c) - r_c^2 f''(r_c)]}{2r_c^2}}. \quad (25)$$

Here,  $\Omega_c$  is the angular velocity and  $\lambda_L$  is the Lyapunov exponent of the unstable circular null geodesics. The radius of the circular null geodesic, denoted as  $r_c$ , satisfies the condition  $2f(r_c) = r_c f'(r_c)$ . In Fig. 7, we plot the the real and negative imaginary parts of the QNM frequencies in the eikonal limit. With an increase in the parameter  $\gamma$ , there is a monotonic decrease in both the real part and the negative imaginary part of the QNM frequencies, consistent with the results shown in Fig. 6. In fact, the relationship between the angular velocity  $\Omega_c$  in Eq. (25) and the shadow radius  $\mathcal{R}_{sh}$  in Eq. (17) is given by [60, 65, 120, 121]

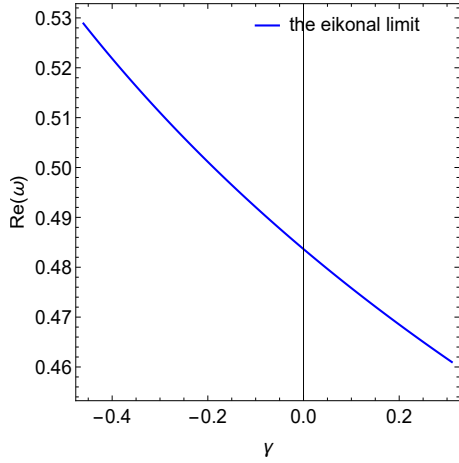
$$\mathcal{R}_{sh} = \frac{1}{\Omega_c} = \frac{r_c}{\sqrt{f(r_c)}}. \quad (26)$$

Using Eq. (26), we plot the shadow radius  $\mathcal{R}_{sh}$  for different values of the parameter  $\gamma$  in Fig. 8. As the parameter  $\gamma$  increases, the shadow radius  $\mathcal{R}_{sh}$  exhibits a monotonic increase, which is opposite to the trends observed of the real parts in Figs. 6 and 7.

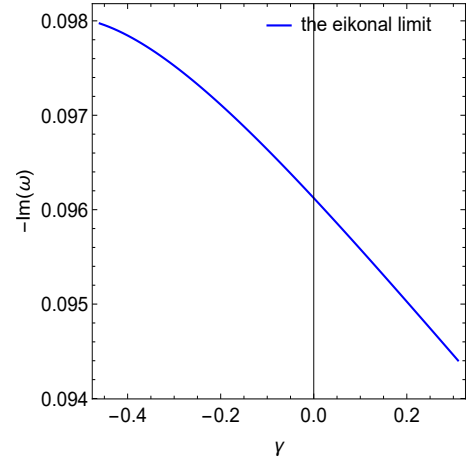
Moreover, the oscillation frequencies for M87\* and SgrA\* can be converted to values in Hertz as follows:

$$f = \frac{\text{Re}(\omega)}{2\pi M} \times \frac{c^3}{G}, \quad (27)$$

where  $\text{Re}(\omega)$  is the real part of the QNM frequency,  $M$  denotes the mass of the supermassive BH,  $c = 3 \times 10^8$  m/s is the speed of light, and  $G = 6.67430 \times 10^{-11}$  m<sup>3</sup> kg<sup>-1</sup> s<sup>-2</sup> is the gravitational constant. By taking  $M_{M87^*} = 6.5 \times 10^9 M_\odot$  and  $M_{\text{Sgr.A}^*} = 4.3 \times 10^6 M_\odot$  (where the solar mass  $M_\odot = 1.989 \times 10^{30}$  kg), we plot the oscillation frequencies in Hertz for the supermassive BHs M87\* and SgrA\* in Fig. 9. We find that the oscillation frequencies of a fundamental mode ( $n = 0$  and  $\ell = 2$ ) of M87\* and SgrA\* both monotonically decrease with the increase of the parameter  $\gamma$ . For M87\*, the frequency range is  $2.4 \times 10^{-6} \text{ Hz} \lesssim f \lesssim 2.7 \times 10^{-6} \text{ Hz}$ . And for SgrA\*, the frequency



(a) The real parts of QNM frequencies.



(b) The negative imaginary parts of QNM frequencies.

Figure 7: The real and negative imaginary parts of the QNM frequencies calculated via the eikonal limit. The parameter  $-0.46 \lesssim \gamma \lesssim 0.31$  at  $1\sigma$  confidence interval based on the EHT data. We set the overtone number  $n = 0$ , the multipole number  $\ell = 2$ , and  $M = 1$ .

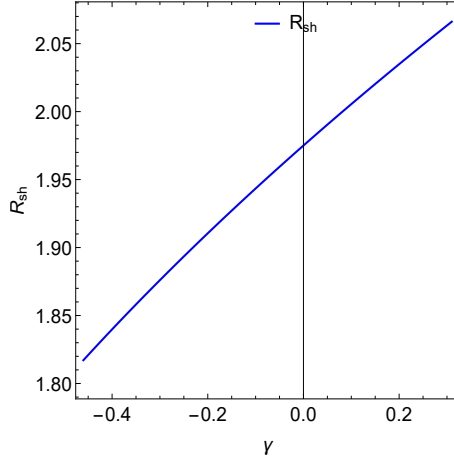


Figure 8: the shadow radius  $R_{\text{sh}}$  with different parameter  $\gamma$ . The parameter  $-0.46 \lesssim \gamma \lesssim 0.31$  at  $1\sigma$  confidence interval based on the EHT data. We set  $M = 1$ .

range is  $3.6 \times 10^{-3} \text{Hz} \lesssim f \lesssim 4.1 \times 10^{-3} \text{Hz}$ . The result reveals a negative correlation between the mass of a BH and its corresponding frequency.

## 4 Observational appearances of the BH in Horndeski theory

In this section, we investigate the optical appearances of the BH in Horndeski theory, which is encircled by an optically and geometrically thin disk. Additionally, we analyze the impact of the parameter  $\gamma$  on these optical appearances.

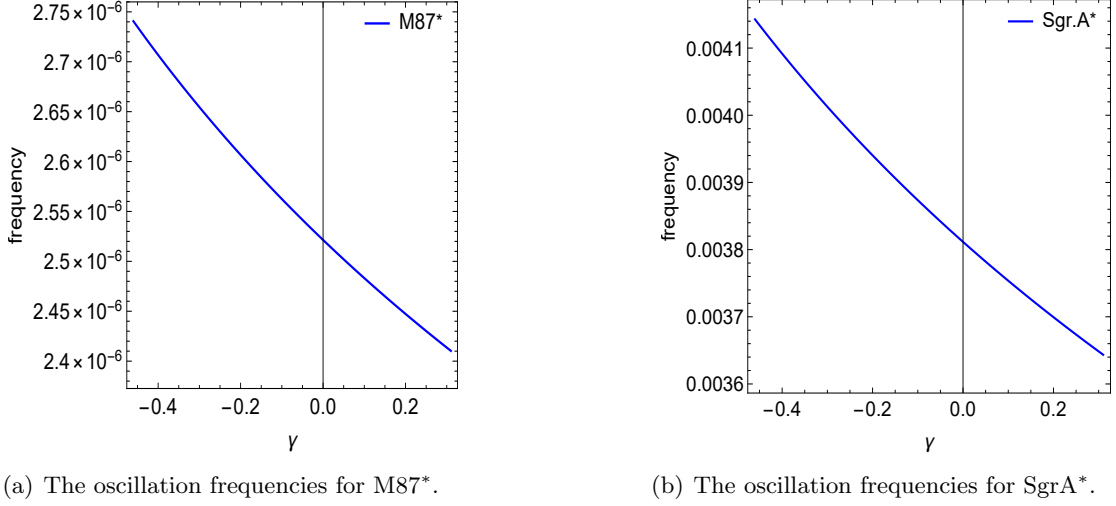


Figure 9: The oscillation frequencies of the supermassive BHs M87\* and SgrA\* for various values of the parameter  $\gamma$ . The parameter  $-0.46 \lesssim \gamma \lesssim 0.31$  at  $1\sigma$  confidence interval based on the EHT data. We set the overtone number  $n = 0$ , the multipole number  $\ell = 2$ .

#### 4.1 Direct emission, photon ring, and lensing ring

To investigate the optical appearances of the BH in Horndeski theory, we consider the BH's equatorial plane to be fixed, with the static observer and the light source positioned at infinity in the north pole and south pole directions, respectively. We then use  $n \equiv \phi/(2\pi)$  to represent the total number of orbits the photons make around the BH. Based on the value of  $n$ , we can classify the light rays into the following three categories [20]:

- *Direct Emission:*  $n < 3/4$ . Light rays intersect the equatorial plane at most once;
- *Lensing Ring:*  $3/4 < n < 5/4$ . Light rays intersect the equatorial plane twice;
- *Photon Ring:*  $n > 5/4$ . Light rays intersect the equatorial plane at least three times.

We have plotted the relationship between the total number of orbits  $n$  and the impact parameter  $b$  for different values of the parameter  $\gamma = -0.3, 0, 0.3$ , as shown in Fig. 10. The graph is divided into three regions: "Direct Emission," "Lensing Ring," and "Photon Ring," corresponding to the three categories of light rays mentioned above. These regions are separated by horizontal dashed lines at  $n = 3/4$  and  $n = 5/4$ , representing the total number of orbits. For the blue curve in Fig. 10, we set the parameter  $\gamma = -0.3$ . We observe that the total number of orbits  $n$  increases with the impact parameter  $b/M$ , reaching a peak at approximately  $b/M \approx 4.9$ . After this point, the total number of orbits  $n$  decreases rapidly to  $n = 5/4$ , and then gradually decreases, approaching  $n = 1/2$ . This behavior indicates that as  $b/M$  continues to increase, the deflection of light rays diminishes, and their paths eventually approximate a straight line. Additionally, in Tab 1, we present the ranges of the impact parameter corresponding to the direct emission, lensing ring, and photon ring for different values of the parameter  $\gamma = -0.3, 0, 0.3$ . When comparing this result with the cases where the parameter  $\gamma = 0$  (the black curve in Fig. 10) and  $\gamma = 0.3$  (the red curve in Fig. 10), we find that the behavior pattern of the total number of orbits  $n$  remains consistent across different parameter  $\gamma$ . However, the larger parameter  $\gamma$  shifts the peak of the total number of orbits  $n$  further along the positive horizontal axis. This indicates that the size of the photon ring increases with the parameter  $\gamma$ .

Parameter $\gamma$	Direct Emission	Lensing Ring	Photon Ring
-0.3	$b/M \notin (4.720, 5.948)$	$b/M \in (4.720, 4.908)$ or $b/M \in (4.950, 5.948)$	$b/M \in (4.908, 4.950)$
0	$b/M \notin (5.014, 6.181)$	$b/M \in (5.014, 5.187)$ or $b/M \in (5.231, 6.181)$	$b/M \in (5.187, 5.231)$
0.3	$b/M \notin (5.272, 6.422)$	$b/M \in (5.272, 5.435)$ or $b/M \in (5.461, 6.422)$	$b/M \in (5.435, 5.461)$

Table 1: Table showing ranges of the impact parameter  $b$  corresponding to the direct emission, lensing ring, and photon ring for the parameter  $\gamma = -0.3, 0, 0.3$ . We set  $M = 1$ .

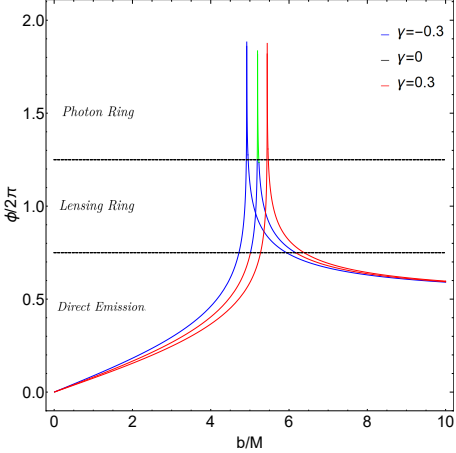


Figure 10: The relationship between the total number of orbits of photons  $n \equiv \phi/(2\pi)$  and the impact parameter  $b/M$  for the BH in Horndeski theory. The blue, black, and red curves correspond to  $\gamma = -0.3$ ,  $\gamma = 0$ , and  $\gamma = 0.3$ , respectively. We set  $M = 1$  and the spacing of the impact parameters for the direct emission, lensing ring, and photon ring are set to  $1/5$ ,  $1/100$ , and  $1/1000$ , respectively.

In addition, we have plotted the trajectories of photons with different impact parameters  $b/M$  in polar coordinates  $(r, \phi)$  in Fig. 11. In this figure, the black disk represents the BH in Horndeski theory, the red ring indicates the photon sphere, and the vertical black line passing through the origin denotes the equatorial plane. The observer is positioned at infinity in the north polar direction, corresponding to the right side of the panel. Taking Fig. 11(a) with the parameter  $\gamma = -0.3$  as an example, we observe that for an observer positioned in the north polar direction, the direct image occupies a significant portion of the observed appearance of the BH (see red curves in Fig. 11(a)), divided into upper and lower sections based on the value of the impact parameter  $b/M$ . In the upper section, photons with larger impact parameters intersect the equatorial plane only once, satisfying  $1/4 < n < 3/4$ . In the lower section, photons can be categorized into two types based on their impact parameters. Photons with relatively larger impact parameters intersect the equatorial plane once before falling into the BH, while those with smaller impact parameters fall into the black hole before intersecting the equatorial plane, satisfying  $n < 1/4$ . Additionally, it can be observed that the lensing ring occupies a smaller central region of the observed appearance (see blue curves in Fig. 11(a)), and is similarly divided into upper and lower sections based on the value of the impact parameter. These photons intersect the equatorial plane twice, with the distance between the two points of intersection increasing as the impact parameter increases. The distinction lies in that the upper photons will escape the BH, while the lower photons will fall into the BH. For the photon ring, we observe that it occupies only a very narrow region of the observed appearance (see

green curves in Fig. 11(a)). The corresponding photons intersect the equatorial plane more than three times. When comparing the results with the cases where the parameters  $\gamma = 0$  (see Fig. 11(b)) and  $\gamma = 0.3$  (see Fig. 11(c)), we find that the behavior pattern of trajectories of photons remains consistent across different impact parameters  $b/M$ . However, a larger value of the parameter  $\gamma$  causes the radii of the black disk and the photon sphere to increase (see Figs. 11(a), 11(b), and 11(c)).

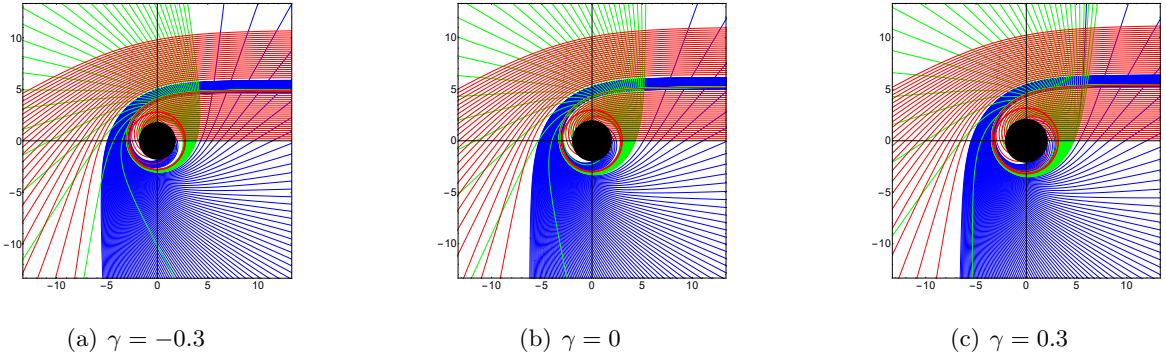


Figure 11: Trajectories of photons near the BH in polar coordinates  $(r, \phi)$ . The black disk represents the BHs with the different parameter  $\gamma = -0.3, 0, 0.3$  in Horndeski theory, the red ring indicates the photon sphere, and the vertical black line passing through the origin denotes the equatorial plane. The red curves, blue curves and green curves represent the direct emission, lensing ring, and photon ring, respectively. We set  $M = 1$ .

## 4.2 Transfer functions

We now consider a BH surrounded by an optically and geometrically thin disk. This disk is located on the equatorial plane and emits isotropically within a static observer's rest frame, while the observer is positioned at the North Pole. The emitted specific intensity is given by [20]

$$I_\nu^{\text{em}} = I(r), \quad (28)$$

in which  $\nu$  represents the emission frequency in the static frame. Considering that  $I_\nu/\nu^3$  remains conserved along the ray, we can derive the specific intensity of the radiation emitted from a radius  $r$  and received at any frequency  $\nu'$ , which is

$$I_{\nu'}^{\text{obs}} = f(r)^{3/2} I(r). \quad (29)$$

Then we can obtain the total specific intensity as follows:

$$I^{\text{obs}} = \int I_{\nu'}^{\text{obs}} d\nu' = \int f^2(r) I_\nu^{\text{em}} d\nu = f(r)^2 I(r). \quad (30)$$

Since we are considering an optically and geometrically thin disk located on the equatorial plane, each time a photon intersects this plane, it acquires brightness from the disk's emission, as shown in Fig. 11. Consequently, the observed intensity is given by

$$I^{\text{obs}}(b) = \sum_n f(r)^2 I \Big|_{r=r_n(b)}. \quad (31)$$

Here,  $r_n(b)$  ( $n = 1, 2, 3, \dots$ ) is the transfer function, representing the radial coordinate of the  $n$ -th intersection point between the photon and the thin accretion disk. The slope of the function  $r_n(b)$  at each value of  $b$  yields the demagnification factor at that point, denoted as  $dr/db$ . In Fig. 12, we have plotted the first three transfer functions for different values of the parameter  $\gamma = -0.3, 0, 0.3$ . Taking  $\gamma = -0.3$  as an example, we observe that the transfer functions do not support  $b \lesssim 2.63M$ . This value is greater than the event horizon radius ( $r_h \approx 1.84M$ ) but smaller than the photon sphere radius ( $r_{ph} \approx 2.78M$ ). The first transfer function ( $n = 1$ ) corresponds to the direct emission (see red line in Fig. 12(a)), with a slope close to 1, essentially representing a redshifted source image of the thin accretion disk. The second transfer function ( $n = 2$ ) pertains to the lensed ring (see blue curve in Fig. 12(a)), with a steeper slope, providing a reduced image of the thin accretion disk's back side. The third transfer function ( $n = 3$ ) is associated with the photon ring (see green curve in Fig. 12(a)), having the steepest slope, and offers a highly reduced image of the thin accretion disk's front side. This implies that the first transfer function, representing the direct emission, contributes the most to the total flux, while the second transfer function, representing the lensed ring, contributes less. The third transfer function, representing the photon ring, contributes very little to the total flux. For the cases  $\gamma = 0$  (see Fig. 12(b)) and  $\gamma = 0.3$  (see Fig. 12(c)), we find that the behavior pattern of the transfer functions remains consistent. However, a larger value of the parameter  $\gamma$  results in an increased initial  $b/M$  value for the transfer functions.

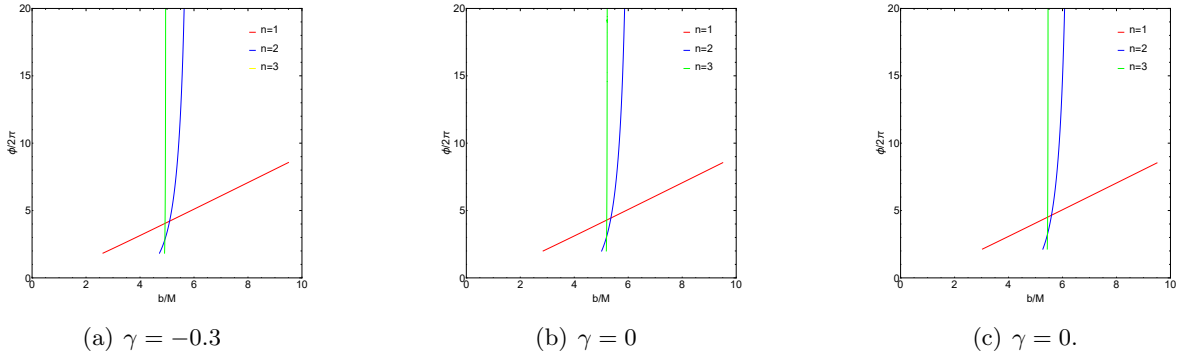


Figure 12: The first three transfer functions of the BH in Horndeski theory for various values of the parameter  $\gamma$ . The red, blue, and green curves represent the radial coordinates of the photons at their first, second, and third intersections with the thin accretion disk, respectively. We set  $M = 1$  and  $\gamma = -0.3, 0, 0.3$ .

### 4.3 Optical appearances of the BH with three emission models of the thin accretion disk

In this section, we investigate the optical appearances of the BH using three specific thin accretion disk emission models, as illustrated in Fig. 13. The first emission model can be expressed as

$$I_1^{\text{em}}(r) = \begin{cases} I_0 \left[ \frac{1}{r - (r_{\text{isco}} - 1)} \right]^2, & r > r_{\text{isco}}, \\ 0, & r \leq r_{\text{isco}}. \end{cases} \quad (32)$$

Here, we assume that the emission starts from the innermost stable circular orbit  $r_{\text{isco}}$ , where it suddenly increases, reaches a peak, and then rapidly declines, as shown in Fig. 13(a). The second

emission model assumes that the emission starts from the event horizon and decays towards the innermost stable circular orbit at a slower rate compared to the first emission model. As shown in Fig. 13(b), the emitted specific intensity of the second emission model is given by

$$I_2^{\text{em}}(r) = \begin{cases} I_0 \frac{\frac{\pi}{2} - \arctan[r - (r_{\text{isco}} - 1)]}{\frac{\pi}{2} - \arctan[r_h - (r_{\text{isco}} - 1)]}, & r > r_h, \\ 0, & r \leq r_h. \end{cases} \quad (33)$$

In the third emission model, the emission is assumed to occur at the photon sphere radius  $r_{\text{ph}}$  and then rapidly decay at a cubic rate, as shown in Fig. 13(c). The emitted specific intensity is given by

$$I_3^{\text{em}}(r) = \begin{cases} I_0 \left[ \frac{1}{r - (r_{\text{ph}} - 1)} \right]^3, & r > r_{\text{ph}}, \\ 0, & r \leq r_{\text{ph}}. \end{cases} \quad (34)$$

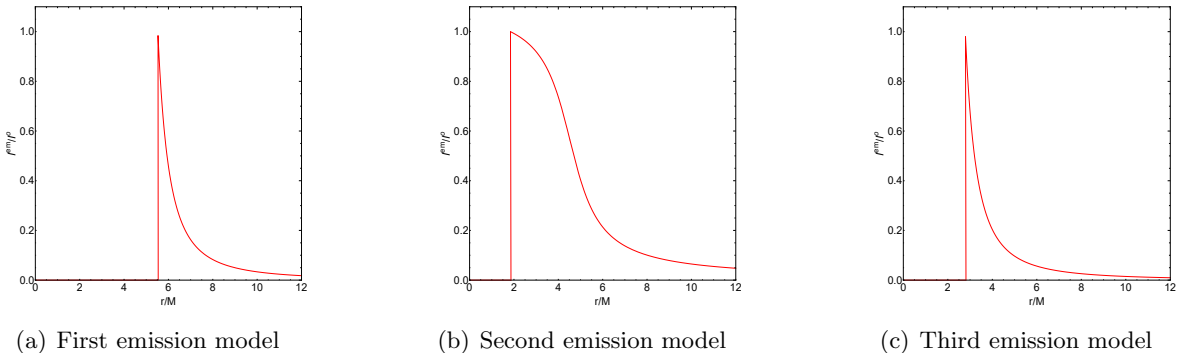


Figure 13: Emitted intensity of the thin accretion disk for the three emission models.

Combining the observed intensity (31) and three emission models (32-34), we present the optical appearances of a BH in Horndeski theory with the parameter  $\gamma = -0.3$ , as shown in Fig. 14. For the first emission model (illustrated in Fig. 14(a)), we observe that the observed specific intensity has a peak at  $b/M \approx 6.43$ , corresponding to the direct emission. At  $b/M \approx 5.24$ , there is a narrow peak in the observed specific intensity, corresponding to the lensing ring. Additionally, at the far left of Fig. 14 around  $b/M \approx 4.95$ , there is an extremely narrow peak in the observed specific intensity, corresponding to the photon ring. As shown in Fig. 14(d), we also present the two-dimensional image of the BH as observed by a north polar observer under the first emission model. We find a bright ring at the outer edge of the two-dimensional image that gradually diminishes in intensity outward, known as the direct emission. The demagnification factor for the first transfer function corresponding to the direct emission is close to 1, contributing the majority of the total flux. In the dark region of the two-dimensional image center, there is a narrow bright ring representing the lensing ring. The demagnification factor for the second transfer function corresponding to the lensing ring is relatively large, contributing a smaller portion of the total flux. Additionally, at the innermost part of the two-dimensional image, there is a very narrow ring known as the photon ring. The demagnification factor for the third transfer function corresponding to the photon ring is extremely large, contributing minimally to the total flux, which makes the photon ring less prominent in the two-dimensional image. The observed specific intensity for the second emission model is shown in Fig. 14(b). We find that the direct emission appears at  $b/M \approx 2.66$ , and the lensed ring overlaps with the direct emission at  $b/M \approx 4.74$ . From the two-dimensional image

of the BH shown in Fig. 14(e), we can also clearly see that the brightness of the two-dimensional image appears at  $b/M \approx 2.66$  and increases with radius, with a brighter lensing ring at  $b/M \approx 4.74$ . The observed specific intensity for the third emission model is shown in Fig. 14(c). We find that the direct emission appears with a lower (compared to Fig. 14(a) and 14(b)) observed intensity at  $b/M \approx 3.61$ , and the lensing ring appears at  $b/M \approx 4.94$ , overlapping with the direct emission and having a peak intensity greater than that of the direct emission. As seen in Fig. 14(f), the brightness of the two-dimensional image of the BH suddenly appears at  $b/M \approx 3.61$  and decreases, until it increases again at  $b/M \approx 4.94$ , before subsequently decreasing with increasing radius. Compared to the first and second emission models, the emitted specific intensity of the third emission model, which starts at the event horizon, results in a dimmer two-dimensional image observed due to the redshift effect.

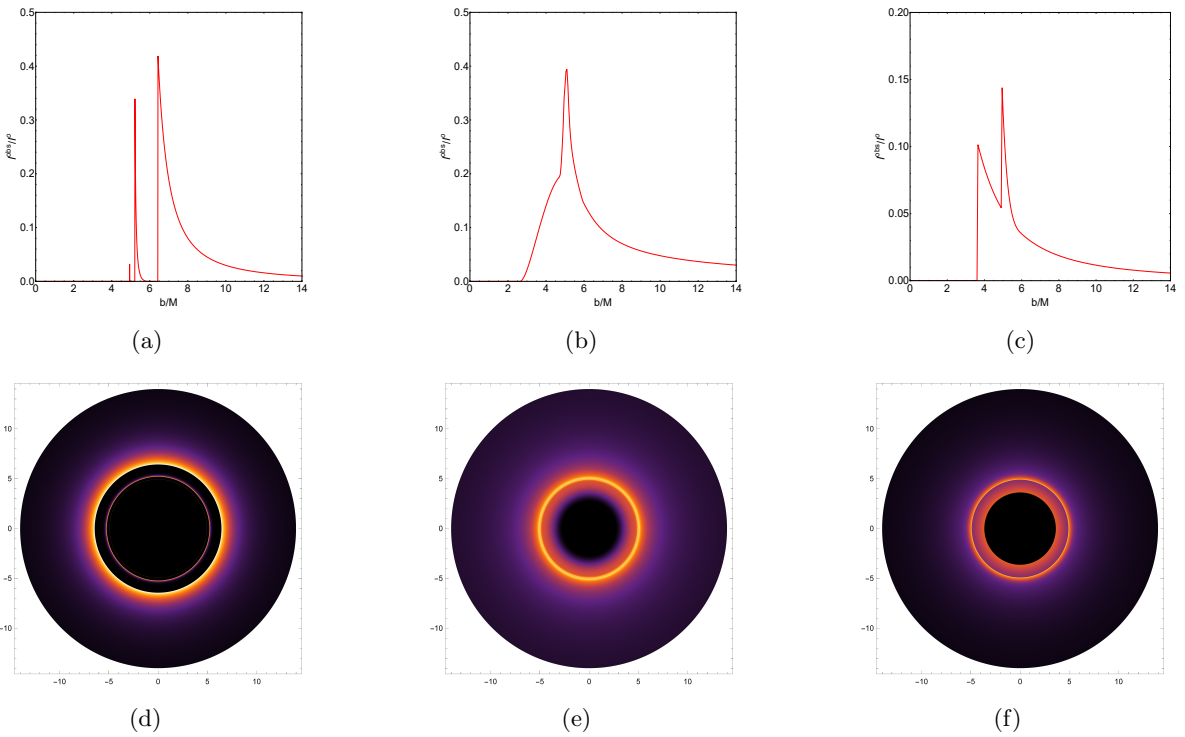


Figure 14: Observed specific intensities and two-dimensional images of the BH in Horndeski theory with three emission models of the thin accretion disk. We set  $M = 1$  and the parameter  $\gamma = -0.3$ .

To facilitate a comparison with the BH images provided by the EHT, we applied a Gaussian filter with a width of  $20\mu\text{as}$  to the images in Figs. 14(d), 14(e), and 14(f) [8, 122, 123], as shown in Figs. 15. It can be observed that the filter removes the features of the lensing ring and the photon ring, leaving only a blurred image of the direct emission, with its size remaining unchanged. This indicates that, at the current resolution of the EHT, it is challenging to obtain information about the lensing ring and photon ring in the BH image. Therefore, the actual appearance of the BH image largely depends on the structure of the thin accretion disk itself.

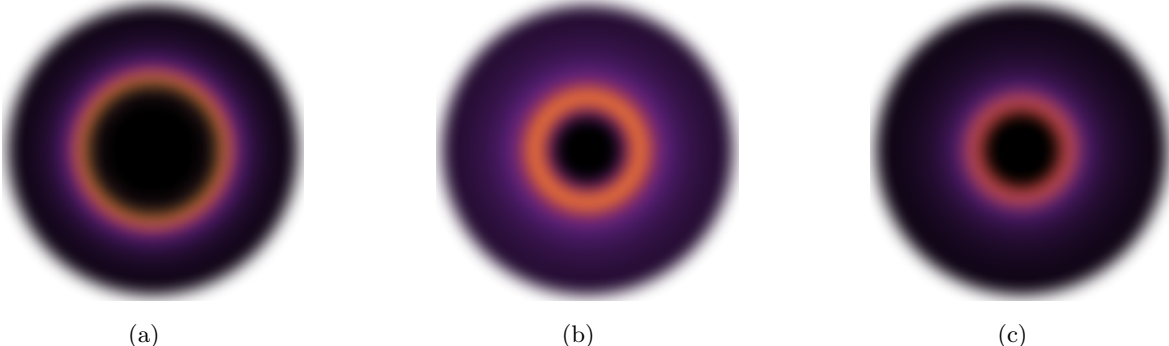


Figure 15: Blurred two-dimensional images with a Gaussian filter with a width of  $20\mu\text{as}$ .

## 5 Conclusions

In this paper, we investigate the motion of photons in the spacetime background of the BH in Horndeski theory, the QNMs of the BH, and the optical appearances of the BH surrounded by an optically and geometrically thin accretion disk.

First, we analyze the motion of photons in the BH spacetime background, deriving the effective potential, critical impact parameter, and photon sphere radius. We find that as the parameter  $\gamma$  increases, the critical impact parameter, photon sphere radius, and event horizon radius also increase. This implies that the size of the photon sphere can expand outward with the increasing parameter  $\gamma$ . We also plot the scenarios where photons with impact parameters smaller and larger than the critical impact parameter are absorbed and reflected by the BH, respectively. We obtain the expression for the BH shadow radius and use the EHT observational data for M87\* and SgrA\* to constrain the parameter  $\gamma$ . Within a  $1\sigma$  confidence interval, the parameter  $\gamma$  must satisfy certain conditions. M87\* and SgrA\* provide better constraints on Horndeski gravity at the upper and lower limits of the parameter  $\gamma$ , respectively.

Next, we study the perturbations of a scalar field in the black hole background and use the WKB method to calculate its QNMs. Based on EHT data for M87\* and SgrA\*, we compute the QNMs for different values of the parameter  $\gamma$  within the  $1\sigma$  confidence interval. We find that as the parameter  $\gamma$  increases, both the real part and the negative imaginary part decrease monotonically. This implies that a smaller parameter  $\gamma$  corresponds to higher oscillation frequencies of the scalar waves. Additionally, we analyze the QNMs in the eikonal limit and find that as the parameter  $\gamma$  increases, the real part and the negative imaginary part of the QNMs decrease monotonically. However, as the parameter  $\gamma$  increases, the shadow radius shows a monotonically increasing trend, which is opposite to the observed change in the real part of the QNMs. We also calculate the frequency range of the fundamental mode of M87\* and SgrA\* within the  $1\sigma$  confidence interval, constrained to  $2.4 \times 10^{-6}\text{Hz} \lesssim f \lesssim 2.7 \times 10^{-6}\text{Hz}$  and  $3.6 \times 10^{-3}\text{Hz} \lesssim f \lesssim 4.1 \times 10^{-3}\text{Hz}$ , respectively.

Finally, we examine the optical appearances of the BH surrounded by a thin accretion disk. Based on the total number of orbits, we classify the light rays into three categories: direct emission, lensing ring, and photon ring. Each intersection of the photon with the accretion disk increases its brightness. Under different values of the parameter  $\gamma$ , we calculate the range of the impact parameter corresponding to the direct emission, lensing ring, and photon ring, respectively. We find that larger values of the parameter  $\gamma$  shift the peak of the total number of orbits further along the positive horizontal axis. This indicates that the sizes of the direct emission, lensing ring, and

photon ring increase with an increasing  $\gamma$ . By analyzing the first three transfer functions under the different parameter  $\gamma$ , we find that the first transfer function corresponds to a direct emission with a demagnification factor close to 1, indicating the redshift effect of the accretion disk and contributing the majority of the total flux. The second transfer function corresponds to the lensing ring, with a larger demagnification factor, producing a reduced image of the back side of the disk and contributing a smaller portion of the total flux. The third transfer function corresponds to the photon ring, with an extremely large demagnification factor, producing a highly reduced image of the front side of the disk and contributing minimally to the total flux. Using the above analysis, we study the optical appearances of the BH under three emission models, with emissions starting at the innermost stable circular orbit, event horizon radius, and photon sphere radius, respectively. In the first emission model, we find that the direct emission, lensing ring, and photon ring are distinct. In the second and third emission models, we find no photon ring, and the lensing ring overlaps with the direct emission. This indicates that the optical appearances of the BH depends on the choice of the emission model. We apply a Gaussian filter with a width of  $20\mu\text{as}$  to the BH's optical appearance and compare it with the image provided by the EHT. We find that the filter removes the features of the lensing ring and photon ring, leaving only a blurred direct emission whose size remains unchanged. This suggests that, given the current resolution of the EHT, it is challenging to obtain detailed information about the lensing ring and photon ring, and the actual image of the BH is largely influenced by the structure of the accretion disk. In future research, we aim to extend the analysis to rotating BHs to impose stricter constraints on the parameter  $\gamma$ .

### Acknowledgments

This work was supported by the National Key Research and Development Program of China (Grant No. 2021YFC2203004), the Natural Science Foundation of Chongqing (Grant No. CSTB2023NSCQ-MSX0103), and the National Natural Science Foundation of China (Grant No. 12347101).

## References

- [1] B. P. Abbott *et al.* [LIGO Scientific and Virgo], Phys. Rev. Lett. **116**, no.6, 061102 (2016) doi:10.1103/PhysRevLett.116.061102 [arXiv:1602.03837 [gr-qc]].
- [2] B. P. Abbott *et al.* [LIGO Scientific and Virgo], Phys. Rev. Lett. **116**, no.24, 241102 (2016) doi:10.1103/PhysRevLett.116.241102 [arXiv:1602.03840 [gr-qc]].
- [3] B. P. Abbott *et al.* [LIGO Scientific and Virgo], Phys. Rev. Lett. **116**, no.24, 241103 (2016) doi:10.1103/PhysRevLett.116.241103 [arXiv:1606.04855 [gr-qc]].
- [4] B. P. Abbott *et al.* [LIGO Scientific and VIRGO], Phys. Rev. Lett. **118**, no.22, 221101 (2017) [erratum: Phys. Rev. Lett. **121**, no.12, 129901 (2018)] doi:10.1103/PhysRevLett.118.221101 [arXiv:1706.01812 [gr-qc]].
- [5] B. P. Abbott *et al.* [LIGO Scientific and Virgo], Phys. Rev. Lett. **119**, no.14, 141101 (2017) doi:10.1103/PhysRevLett.119.141101 [arXiv:1709.09660 [gr-qc]].
- [6] B. P. Abbott *et al.* [LIGO Scientific and Virgo], Astrophys. J. Lett. **851**, L35 (2017) doi:10.3847/2041-8213/aa9f0c [arXiv:1711.05578 [astro-ph.HE]].
- [7] B. P. Abbott *et al.* [LIGO Scientific and Virgo], Phys. Rev. Lett. **119**, no.16, 161101 (2017) doi:10.1103/PhysRevLett.119.161101 [arXiv:1710.05832 [gr-qc]].
- [8] K. Akiyama *et al.* [Event Horizon Telescope], Astrophys. J. Lett. **875**, L1 (2019) doi:10.3847/2041-8213/ab0ec7 [arXiv:1906.11238 [astro-ph.GA]].

- [9] K. Akiyama *et al.* [Event Horizon Telescope], *Astrophys. J. Lett.* **875**, no.1, L2 (2019) doi:10.3847/2041-8213/ab0c96 [arXiv:1906.11239 [astro-ph.IM]].
- [10] K. Akiyama *et al.* [Event Horizon Telescope], *Astrophys. J. Lett.* **875**, no.1, L3 (2019) doi:10.3847/2041-8213/ab0c57 [arXiv:1906.11240 [astro-ph.GA]].
- [11] K. Akiyama *et al.* [Event Horizon Telescope], *Astrophys. J. Lett.* **875**, no.1, L4 (2019) doi:10.3847/2041-8213/ab0e85 [arXiv:1906.11241 [astro-ph.GA]].
- [12] K. Akiyama *et al.* [Event Horizon Telescope], *Astrophys. J. Lett.* **875**, no.1, L5 (2019) doi:10.3847/2041-8213/ab0f43 [arXiv:1906.11242 [astro-ph.GA]].
- [13] K. Akiyama *et al.* [Event Horizon Telescope], *Astrophys. J. Lett.* **875**, no.1, L6 (2019) doi:10.3847/2041-8213/ab1141 [arXiv:1906.11243 [astro-ph.GA]].
- [14] K. Akiyama *et al.* [Event Horizon Telescope], *Astrophys. J. Lett.* **930**, no.2, L12 (2022) doi:10.3847/2041-8213/ac6674 [arXiv:2311.08680 [astro-ph.HE]].
- [15] K. Akiyama *et al.* [Event Horizon Telescope], *Astrophys. J. Lett.* **930**, no.2, L13 (2022) doi:10.3847/2041-8213/ac6675 [arXiv:2311.08679 [astro-ph.HE]].
- [16] K. Akiyama *et al.* [Event Horizon Telescope], *Astrophys. J. Lett.* **930**, no.2, L14 (2022) doi:10.3847/2041-8213/ac6429 [arXiv:2311.09479 [astro-ph.HE]].
- [17] K. Akiyama *et al.* [Event Horizon Telescope], *Astrophys. J. Lett.* **930**, no.2, L15 (2022) doi:10.3847/2041-8213/ac6736 [arXiv:2311.08697 [astro-ph.HE]].
- [18] K. Akiyama *et al.* [Event Horizon Telescope], *Astrophys. J. Lett.* **930**, no.2, L16 (2022) doi:10.3847/2041-8213/ac6672 [arXiv:2311.09478 [astro-ph.HE]].
- [19] K. Akiyama *et al.* [Event Horizon Telescope], *Astrophys. J. Lett.* **930**, no.2, L17 (2022) doi:10.3847/2041-8213/ac6756 [arXiv:2311.09484 [astro-ph.HE]].
- [20] S. E. Gralla, D. E. Holz and R. M. Wald, *Phys. Rev. D* **100**, no.2, 024018 (2019) doi:10.1103/PhysRevD.100.024018 [arXiv:1906.00873 [astro-ph.HE]].
- [21] V. Perlick and O. Y. Tsupko, *Phys. Rept.* **947**, 1-39 (2022) doi:10.1016/j.physrep.2021.10.004 [arXiv:2105.07101 [gr-qc]].
- [22] J. L. Synge, *Mon. Not. Roy. Astron. Soc.* **131**, no.3, 463-466 (1966). doi:10.1093/mnras/131.3.463
- [23] J. P. Luminet, *Astron. Astrophys.* **75**, 228-235 (1979).
- [24] J. M. Bardeen, Proceedings, Ecole d'Eté de Physique Théorique: Les Astres Occlus : Les Houches, France, August, 1972, 215-240, 215-240 (1973).
- [25] K. Hioki and U. Miyamoto, *Phys. Rev. D* **78**, 044007 (2008) doi:10.1103/PhysRevD.78.044007 [arXiv:0805.3146 [gr-qc]].
- [26] E. F. Eiroa and C. M. Sendra, *Eur. Phys. J. C* **78**, no.2, 91 (2018) doi:10.1140/epjc/s10052-018-5586-6 [arXiv:1711.08380 [gr-qc]].
- [27] L. Amarilla, E. F. Eiroa and G. Giribet, *Phys. Rev. D* **81**, 124045 (2010) doi:10.1103/PhysRevD.81.124045 [arXiv:1005.0607 [gr-qc]].
- [28] L. Amarilla and E. F. Eiroa, *Phys. Rev. D* **85**, 064019 (2012) doi:10.1103/PhysRevD.85.064019 [arXiv:1112.6349 [gr-qc]].
- [29] L. Amarilla and E. F. Eiroa, *Phys. Rev. D* **87**, no.4, 044057 (2013) doi:10.1103/PhysRevD.87.044057 [arXiv:1301.0532 [gr-qc]].

- [30] M. Amir, B. P. Singh and S. G. Ghosh, Eur. Phys. J. C **78**, no.5, 399 (2018) doi:10.1140/epjc/s10052-018-5872-3 [arXiv:1707.09521 [gr-qc]].
- [31] B. P. Singh and S. G. Ghosh, Annals Phys. **395**, 127-137 (2018) doi:10.1016/j.aop.2018.05.010 [arXiv:1707.07125 [gr-qc]].
- [32] Y. Mizuno, Z. Younsi, C. M. Fromm, O. Porth, M. De Laurentis, H. Olivares, H. Falcke, M. Kramer and L. Rezzolla, Nature Astron. **2**, no.7, 585-590 (2018) doi:10.1038/s41550-018-0449-5 [arXiv:1804.05812 [astro-ph.GA]].
- [33] S. Vagnozzi and L. Visinelli, Phys. Rev. D **100**, no.2, 024020 (2019) doi:10.1103/PhysRevD.100.024020 [arXiv:1905.12421 [gr-qc]].
- [34] I. Banerjee, S. Chakraborty and S. SenGupta, Phys. Rev. D **101**, no.4, 041301 (2020) doi:10.1103/PhysRevD.101.041301 [arXiv:1909.09385 [gr-qc]].
- [35] C. Bambi and K. Freese, Phys. Rev. D **79**, 043002 (2009) doi:10.1103/PhysRevD.79.043002 [arXiv:0812.1328 [astro-ph]].
- [36] C. Bambi and N. Yoshida, Class. Quant. Grav. **27**, 205006 (2010) doi:10.1088/0264-9381/27/20/205006 [arXiv:1004.3149 [gr-qc]].
- [37] F. Atamurotov, A. Abdujabbarov and B. Ahmedov, Phys. Rev. D **88**, no.6, 064004 (2013). doi:10.1103/PhysRevD.88.064004
- [38] U. Papnoi, F. Atamurotov, S. G. Ghosh and B. Ahmedov, Phys. Rev. D **90**, no.2, 024073 (2014) doi:10.1103/PhysRevD.90.024073 [arXiv:1407.0834 [gr-qc]].
- [39] F. Atamurotov and B. Ahmedov, Phys. Rev. D **92**, 084005 (2015) doi:10.1103/PhysRevD.92.084005 [arXiv:1507.08131 [gr-qc]].
- [40] M. Wang, S. Chen and J. Jing, Phys. Rev. D **97**, no.6, 064029 (2018) doi:10.1103/PhysRevD.97.064029 [arXiv:1710.07172 [gr-qc]].
- [41] M. Guo, N. A. Obers and H. Yan, Phys. Rev. D **98**, no.8, 084063 (2018) doi:10.1103/PhysRevD.98.084063 [arXiv:1806.05249 [gr-qc]].
- [42] H. Yan, Phys. Rev. D **99**, no.8, 084050 (2019) doi:10.1103/PhysRevD.99.084050 [arXiv:1903.04382 [gr-qc]].
- [43] R. A. Konoplya, Phys. Lett. B **795**, 1-6 (2019) doi:10.1016/j.physletb.2019.05.043 [arXiv:1905.00064 [gr-qc]].
- [44] C. Bambi, K. Freese, S. Vagnozzi and L. Visinelli, Phys. Rev. D **100**, no.4, 044057 (2019) doi:10.1103/PhysRevD.100.044057 [arXiv:1904.12983 [gr-qc]].
- [45] A. Allahyari, M. Khodadi, S. Vagnozzi and D. F. Mota, JCAP **02**, 003 (2020) doi:10.1088/1475-7516/2020/02/003 [arXiv:1912.08231 [gr-qc]].
- [46] S. Vagnozzi, C. Bambi and L. Visinelli, Class. Quant. Grav. **37**, no.8, 087001 (2020) doi:10.1088/1361-6382/ab7965 [arXiv:2001.02986 [gr-qc]].
- [47] M. Khodadi, A. Allahyari, S. Vagnozzi and D. F. Mota, JCAP **09**, 026 (2020) doi:10.1088/1475-7516/2020/09/026 [arXiv:2005.05992 [gr-qc]].
- [48] S. Vagnozzi, R. Roy, Y. D. Tsai, L. Visinelli, M. Afrin, A. Allahyari, P. Bambhaniya, D. Dey, S. G. Ghosh and P. S. Joshi, *et al.* [arXiv:2205.07787 [gr-qc]].
- [49] N. Tsukamoto, Z. Li and C. Bambi, JCAP **06**, 043 (2014) doi:10.1088/1475-7516/2014/06/043 [arXiv:1403.0371 [gr-qc]].

- [50] N. Tsukamoto, Phys. Rev. D **97**, no.6, 064021 (2018) doi:10.1103/PhysRevD.97.064021 [arXiv:1708.07427 [gr-qc]].
- [51] Z. Hu, Z. Zhong, P. C. Li, M. Guo and B. Chen, Phys. Rev. D **103**, no.4, 044057 (2021) doi:10.1103/PhysRevD.103.044057 [arXiv:2012.07022 [gr-qc]].
- [52] Z. Zhong, Z. Hu, H. Yan, M. Guo and B. Chen, Phys. Rev. D **104**, no.10, 104028 (2021) doi:10.1103/PhysRevD.104.104028 [arXiv:2108.06140 [gr-qc]].
- [53] J. Peng, M. Guo and X. H. Feng, Chin. Phys. C **45**, no.8, 085103 (2021) doi:10.1088/1674-1137/ac06bb [arXiv:2008.00657 [gr-qc]].
- [54] Y. Hou, Z. Zhang, H. Yan, M. Guo and B. Chen, Phys. Rev. D **106**, no.6, 064058 (2022) doi:10.1103/PhysRevD.106.064058 [arXiv:2206.13744 [gr-qc]].
- [55] Y. Hou, M. Guo and B. Chen, Phys. Rev. D **104**, no.2, 024001 (2021) doi:10.1103/PhysRevD.104.024001 [arXiv:2103.04369 [gr-qc]].
- [56] P. V. P. Cunha and C. A. R. Herdeiro, Gen. Rel. Grav. **50**, no.4, 42 (2018) doi:10.1007/s10714-018-2361-9 [arXiv:1801.00860 [gr-qc]].
- [57] V. Ferrari and B. Mashhoon, Phys. Rev. D **30**, 295–304 (1984) doi:10.1103/PhysRevD.30.295
- [58] V. Cardoso, A. S. Miranda, E. Berti, H. Witek and V. T. Zanchin Phys. Rev. D **79**, no.6, 064016 (2009) doi:10.1103/PhysRevD.79.064016 [arXiv:0812.1806 [hep-th]].
- [59] S. Hod, Phys. Rev. D **80**, 064004 (2009) doi:10.1103/PhysRevD.80.064004 [arXiv:0909.0314 [gr-qc]].
- [60] K. Jusufi, Phys. Rev. D **101**, no.8, 084055 (2020) doi:10.1103/PhysRevD.101.084055 [arXiv:1912.13320 [gr-qc]].
- [61] I. Z. Stefanov, S. S. Yazadjiev and G. G. Gyulchev, Phys. Rev. Lett. **104**, 251103 (2010) doi:10.1103/PhysRevLett.104.251103 [arXiv:1003.1609 [gr-qc]].
- [62] Y. Decanini, A. Folacci and B. Jensen, Phys. Rev. D **67**, 124017 (2003) doi:10.1103/PhysRevD.67.124017 [arXiv:gr-qc/0212093 [gr-qc]].
- [63] D. Pedrotti and S. Vagnozzi, [arXiv:2404.07589 [gr-qc]].
- [64] X. C. Cai and Y. G. Miao, Phys. Rev. D **103**, no.12, 124050 (2021) doi:10.1103/PhysRevD.103.124050 [arXiv:2104.09725 [gr-qc]].
- [65] B. Cuadros-Melgar, R. D. B. Fontana and J. de Oliveira, Phys. Lett. B **811**, 135966 (2020) doi:10.1016/j.physletb.2020.135966 [arXiv:2005.09761 [gr-qc]].
- [66] K. Jusufi, M. Amir, M. S. Ali and S. D. Maharaj, Phys. Rev. D **102**, no.6, 064020 (2020) doi:10.1103/PhysRevD.102.064020 [arXiv:2005.11080 [gr-qc]].
- [67] S. H. Hendi, S. N. Sajadi and M. Khademi, Phys. Rev. D **103**, no.6, 064016 (2021) doi:10.1103/PhysRevD.103.064016 [arXiv:2006.11575 [gr-qc]].
- [68] Y. Guo and Y. G. Miao, Phys. Rev. D **102**, no.8, 084057 (2020) doi:10.1103/PhysRevD.102.084057 [arXiv:2007.08227 [hep-th]].
- [69] K. Jusufi, Gen. Rel. Grav. **53**, no.9, 87 (2021) doi:10.1007/s10714-021-02856-6 [arXiv:2007.16019 [gr-qc]].
- [70] K. Jusufi, M. Azreg-Aïnou, M. Jamil, S. W. Wei, Q. Wu and A. Wang, Phys. Rev. D **103**, no.2, 024013 (2021) doi:10.1103/PhysRevD.103.024013 [arXiv:2008.08450 [gr-qc]].
- [71] K. Jusufi, M. Azreg-Aïnou, M. Jamil and T. Zhu, Int. J. Geom. Meth. Mod. Phys. **19**, no.05, 2250068 (2022) doi:10.1142/S0219887822500682 [arXiv:2008.09115 [gr-qc]].

- [72] M. Mondal, A. K. Yadav, P. Pradhan, S. Islam and F. Rahaman, Int. J. Mod. Phys. D **30**, no.12, 2150095 (2021) doi:10.1142/S0218271821500954 [arXiv:2009.03265 [gr-qc]].
- [73] K. Saurabh and K. Jusufi, Eur. Phys. J. C **81**, no.6, 490 (2021) doi:10.1140/epjc/s10052-021-09280-9 [arXiv:2009.10599 [gr-qc]].
- [74] K. Jafarzade, M. Kord Zangeneh and F. S. N. Lobo, Universe **8**, no.3, 182 (2022) doi:10.3390/universe8030182 [arXiv:2009.12988 [gr-qc]].
- [75] K. Jafarzade, M. Kord Zangeneh and F. S. N. Lobo, JCAP **04**, 008 (2021) doi:10.1088/1475-7516/2021/04/008 [arXiv:2010.05755 [gr-qc]].
- [76] M. Ghasemi-Nodehi, M. Azreg-Aïnou, K. Jusufi and M. Jamil, Phys. Rev. D **102**, no.10, 104032 (2020) doi:10.1103/PhysRevD.102.104032 [arXiv:2011.02276 [gr-qc]].
- [77] X. C. Cai and Y. G. Miao, Eur. Phys. J. C **81**, no.6, 559 (2021) doi:10.1140/epjc/s10052-021-09351-x [arXiv:2011.05542 [gr-qc]].
- [78] J. A. V. Campos, M. A. Anacleto, F. A. Brito and E. Passos, Sci. Rep. **12**, no.1, 8516 (2022) doi:10.1038/s41598-022-12343-w [arXiv:2103.10659 [hep-th]].
- [79] M. A. Anacleto, J. A. V. Campos, F. A. Brito and E. Passos, Annals Phys. **434**, 168662 (2021) doi:10.1016/j.aop.2021.168662 [arXiv:2108.04998 [gr-qc]].
- [80] C. Yu, D. Chen and C. Gao, Nucl. Phys. B **983**, 115925 (2022) doi:10.1016/j.nuclphysb.2022.115925 [arXiv:2207.06796 [gr-qc]].
- [81] G. Lambiase, R. C. Pantig, D. J. Gogoi and A. Övgün, Eur. Phys. J. C **83**, no.7, 679 (2023) doi:10.1140/epjc/s10052-023-11848-6 [arXiv:2304.00183 [gr-qc]].
- [82] Q. Gan, P. Wang, H. Wu and H. Yang, Phys. Rev. D **104**, no.4, 044049 (2021) doi:10.1103/PhysRevD.104.044049 [arXiv:2105.11770 [gr-qc]].
- [83] G. S. Bisnovatyi-Kogan and O. Y. Tsupko, Phys. Rev. D **105**, no.6, 064040 (2022) doi:10.1103/PhysRevD.105.064040 [arXiv:2201.01716 [gr-qc]].
- [84] Q. Gan, P. Wang, H. Wu and H. Yang, Phys. Rev. D **104**, no.2, 024003 (2021) doi:10.1103/PhysRevD.104.024003 [arXiv:2104.08703 [gr-qc]].
- [85] P. V. P. Cunha, N. A. Eiró, C. A. R. Herdeiro and J. P. S. Lemos, JCAP **03**, 035 (2020) doi:10.1088/1475-7516/2020/03/035 [arXiv:1912.08833 [gr-qc]].
- [86] S. Guo, G. R. Li and E. W. Liang, Phys. Rev. D **105**, no.2, 023024 (2022) doi:10.1103/PhysRevD.105.023024 [arXiv:2112.11227 [astro-ph.HE]].
- [87] R. Narayan, M. D. Johnson and C. F. Gammie, Astrophys. J. Lett. **885**, no.2, L33 (2019) doi:10.3847/2041-8213/ab518c [arXiv:1910.02957 [astro-ph.HE]].
- [88] X. Qin, S. Chen and J. Jing, Class. Quant. Grav. **38**, no.11, 115008 (2021) doi:10.1088/1361-6382/abf712 [arXiv:2011.04310 [gr-qc]].
- [89] G. W. Horndeski, Int. J. Theor. Phys. **10**, 363-384 (1974) doi:10.1007/BF01807638
- [90] C. Deffayet, G. Esposito-Farese and A. Vikman, Phys. Rev. D **79**, 084003 (2009) doi:10.1103/PhysRevD.79.084003 [arXiv:0901.1314 [hep-th]].
- [91] C. Deffayet, X. Gao, D. A. Steer and G. Zahariade, Phys. Rev. D **84**, 064039 (2011) doi:10.1103/PhysRevD.84.064039 [arXiv:1103.3260 [hep-th]].
- [92] C. Charmousis, E. J. Copeland, A. Padilla and P. M. Saffin, Phys. Rev. Lett. **108**, 051101 (2012) doi:10.1103/PhysRevLett.108.051101 [arXiv:1106.2000 [hep-th]].

- [93] J. Gleyzes, D. Langlois, F. Piazza and F. Vernizzi, Phys. Rev. Lett. **114**, no.21, 211101 (2015) doi:10.1103/PhysRevLett.114.211101 [arXiv:1404.6495 [hep-th]].
- [94] J. Gleyzes, D. Langlois, F. Piazza and F. Vernizzi, JCAP **02**, 018 (2015) doi:10.1088/1475-7516/2015/02/018 [arXiv:1408.1952 [astro-ph.CO]].
- [95] E. Babichev, C. Charmousis and A. Lehébel, JCAP **04**, 027 (2017) doi:10.1088/1475-7516/2017/04/027 [arXiv:1702.01938 [gr-qc]].
- [96] M. Rinaldi, Phys. Rev. D **86**, 084048 (2012) doi:10.1103/PhysRevD.86.084048 [arXiv:1208.0103 [gr-qc]].
- [97] A. Cisterna and C. Erices, Phys. Rev. D **89**, 084038 (2014) doi:10.1103/PhysRevD.89.084038 [arXiv:1401.4479 [gr-qc]].
- [98] A. Anabalón, A. Cisterna and J. Oliva, Phys. Rev. D **89**, 084050 (2014) doi:10.1103/PhysRevD.89.084050 [arXiv:1312.3597 [gr-qc]].
- [99] E. Babichev, C. Charmousis and N. Lecoeur, [arXiv:2309.12229 [gr-qc]].
- [100] C. Charmousis, T. Kolyvaris, E. Papantonopoulos and M. Tsoukalas, JHEP **07**, 085 (2014) doi:10.1007/JHEP07(2014)085 [arXiv:1404.1024 [gr-qc]].
- [101] M. Minamitsuji, Phys. Rev. D **89**, 064017 (2014) doi:10.1103/PhysRevD.89.064017 [arXiv:1312.3759 [gr-qc]].
- [102] E. Babichev, C. Charmousis and A. Lehébel, Class. Quant. Grav. **33**, no.15, 154002 (2016) doi:10.1088/0264-9381/33/15/154002 [arXiv:1604.06402 [gr-qc]].
- [103] X. H. Feng, H. S. Liu, H. Lü and C. N. Pope, JHEP **11**, 176 (2015) doi:10.1007/JHEP11(2015)176 [arXiv:1509.07142 [hep-th]].
- [104] M. Cvetic, G. W. Gibbons and C. N. Pope, Phys. Rev. D **94**, no.10, 106005 (2016) doi:10.1103/PhysRevD.94.106005 [arXiv:1608.02202 [gr-qc]].
- [105] M. Visser, Nucl. Phys. B **328**, 203-212 (1989) doi:10.1016/0550-3213(89)90100-4 [arXiv:0809.0927 [gr-qc]].
- [106] C. Bambi, Phys. Rev. D **87**, 107501 (2013) doi:10.1103/PhysRevD.87.107501 [arXiv:1304.5691 [gr-qc]].
- [107] Z. Chang and Q. H. Zhu, Phys. Rev. D **102**, no.4, 044012 (2020) doi:10.1103/PhysRevD.102.044012 [arXiv:2006.00685 [gr-qc]].
- [108] S. N. Zhang, Front. Phys. (Beijing) **8**, 630-660 (2013) doi:10.1007/s11467-013-0306-z [arXiv:1302.5485 [astro-ph.HE]].
- [109] X. X. Zeng, K. J. He, G. P. Li, E. W. Liang and S. Guo, Eur. Phys. J. C **82**, no.8, 764 (2022) doi:10.1140/epjc/s10052-022-10733-y [arXiv:2209.05938 [gr-qc]].
- [110] X. X. Zeng, K. J. He and G. P. Li, Sci. China Phys. Mech. Astron. **65**, no.9, 290411 (2022) doi:10.1007/s11433-022-1896-0 [arXiv:2111.05090 [gr-qc]].
- [111] K. J. He, X. Zhang and X. Li, Chin. Phys. C **46**, no.7, 075103 (2022) doi:10.1088/1674-1137/ac624a
- [112] R. C. Pantig, L. Mastrototaro, G. Lambiase and A. Övgün, Eur. Phys. J. C **82**, no.12, 1155 (2022) doi:10.1140/epjc/s10052-022-11125-y [arXiv:2208.06664 [gr-qc]].
- [113] V. Perlick, O. Y. Tsupko and G. S. Bisnovatyi-Kogan, Phys. Rev. D **92**, no.10, 104031 (2015) doi:10.1103/PhysRevD.92.104031 [arXiv:1507.04217 [gr-qc]].

- [114] D. Psaltis *et al.* [Event Horizon Telescope], Phys. Rev. Lett. **125**, no.14, 141104 (2020) doi:10.1103/PhysRevLett.125.141104 [arXiv:2010.01055 [gr-qc]].
- [115] B. F. Schutz and C. M. Will, Astrophys. J. Lett. **291**, L33-L36 (1985) doi:10.1086/184453
- [116] S. Iyer and C. M. Will, Phys. Rev. D **35**, 3621 (1987) doi:10.1103/PhysRevD.35.3621
- [117] R. A. Konoplya, Phys. Rev. D **68**, 024018 (2003) doi:10.1103/PhysRevD.68.024018 [arXiv:gr-qc/0303052 [gr-qc]].
- [118] R. A. Konoplya and A. Zhidenko, JCAP **05**, 050 (2017) doi:10.1088/1475-7516/2017/05/050 [arXiv:1705.01656 [hep-th]].
- [119] R. A. Konoplya and Z. Stuchlík, Phys. Lett. B **771**, 597-602 (2017) doi:10.1016/j.physletb.2017.06.015 [arXiv:1705.05928 [gr-qc]].
- [120] H. Lu and H. D. Lyu, Phys. Rev. D **101**, no.4, 044059 (2020) doi:10.1103/PhysRevD.101.044059 [arXiv:1911.02019 [gr-qc]].
- [121] M. Zhang and M. Guo, Eur. Phys. J. C **80**, no.8, 790 (2020) doi:10.1140/epjc/s10052-020-8389-5 [arXiv:1909.07033 [gr-qc]].
- [122] R. Carballo-Rubio, V. Cardoso and Z. Younsi, Phys. Rev. D **106**, no.8, 084038 (2022) doi:10.1103/PhysRevD.106.084038 [arXiv:2208.00704 [gr-qc]].
- [123] D. Psaltis, L. Medeiros, T. R. Lauer, C. K. Chan and F. Ozel, [arXiv:2004.06210 [astro-ph.HE]].